Research Article | Vol. 16, No. 3 / 1 Mar 2026 / Optical Materials Express 692

Optical Materials EXPRESS

Second harmonic enhancement in a hybrid plasmonic-lithium niobate metasurface enabled by guided mode resonances [Invited]

DANIIL ANSIMOV,[1,*] EVIATAR MINERBI,[1,2] MAI TAL,[1,2] MARCO FINAZZI,[3] MICHELE CELEBRANO,[3] AND TAL ELLENBOGEN[1]

[1]*Department of Physical Electronics, School of Electrical and Computer Engineering Tel Aviv University, Tel Aviv 69978, Israel*
[2]*School of Physics and Astronomy, Tel Aviv University, Tel Aviv 6779801, Israel*
[3]*Physics Department, Politecnico di Milano, 20133 Milano, Italy*
[*]*ansimov@mail.tau.ac.il*

Abstract: We study the enhancement of second-harmonic generation (SHG) from a thin lithium niobate film on insulator covered with a gold nanoantenna array. The array is engineered to excite the TE_0 guided mode of the thin film at the fundamental harmonic. By spectrally detuning the localized antenna resonance from the collective guided mode resonance, we achieve control over the resonance quality factor, which enhances the nonlinear interaction. Experimental measurements show a 22-fold enhancement of SHG compared to the bare thin film, an absolute conversion efficiency of 1.35×10^{-5}, and an angular tunability of the guided mode resonance of ~100 nm. The SHG efficiency and linewidth are consistent with the observed collective resonance properties, and are limited mostly by fabrication imperfections. These results emphasize the potential of hybrid plasmonic metasurface-waveguide configurations for integrated photonic applications.

1. Introduction

Second-harmonic generation (SHG) in integrated photonic platforms plays a central role in on-chip frequency conversion, optical signal processing, and emerging quantum technologies. In this framework, one of the leading emerging platforms is lithium niobate on insulator (LNOI) [1–3]. Over the past decades, LNOI thin films have become commercially available, enabled by fabrication techniques such as ion slicing, direct wafer bonding, and chemical–mechanical polishing. In particular, they are well suited for frequency conversion applications due to the high second-order nonlinearity of LN ($d_{33} \approx 30$ pm/V at 1550 nm), high damage thresholds, broad transparency window, and compatibility with on-chip integration [4].

LNOI can be used for SHG in planar photonic circuits or for SHG of free propagating beams. In the first case, conventional waveguides are realized within the thin film. The fundamental light is edge- or grating-coupled to the waveguides, phase matching of the interacting waves is required, and the generated SH signal is collected at the opposite waveguide facet or through an output coupler. Such planar devices have demonstrated very high conversion efficiencies. For example, Li *et al.* employed modal phase matching in a waveguide configuration and demonstrated 83 W^{-1} cm^{-2} normalized efficiency and up to 40% absolute conversion [5]. Periodically poled and birefringently phase-matched waveguides were also investigated and showed a slightly lower but comparable performance [6,7]. In addition, photonic crystal cavities that support ultra-high Q resonances ($Q \approx 3.5 \times 10^5$) and enhance nonlinear interactions were studied [8]. However, such cavities are optimized primarily for the fundamental mode, limiting the overall conversion efficiency [8]. Discussed in-plane geometries usually require complex fabrication processes, such as dry etching of LNOI thin films. One of the proposed methods to address this challenge is

#584523
Journal © 2026

https://doi.org/10.1364/OME.584523
Received 14 Nov 2025; revised 21 Jan 2026; accepted 3 Feb 2026; published 25 Feb 2026

loading the lithium niobate film with CMOS-compatible materials, such as silicon nitride (SiN), which enables the fabrication of waveguides and microring resonators without direct etching of the LN layer [9]. While in-plane devices demonstrate very high conversion efficiencies they have limited spectral tunability, control over the spatial phase profile, shape and polarization of the generated SH.

The second approach utilizes free-propagating beams, where the pump beam is directed onto the LNOI surface at normal incidence or at a certain angle, and the resulting SH signal is collected in transmission. This geometry offers greater design flexibility and enables integration with free-space optics. These properties were used recently to demonstrate LNOI metasurfaces for polarization-dependent SHG beam steering, observation of anapole resonance for SHG enhancement, modulation of SHG, and generation of entangled photons through spontaneous parametric down conversion [10–14]. However, the reduced interaction length results in limited conversion efficiencies. Different configurations that enhance the nonlinear interaction in the thin film were studied in the past, including structured free-standing membranes [15] and plasmonic nanoantenna mediated hot-spots [16].

Another strategy to enhance SHG efficiency in devices operating on the free space beams is to couple the incident light into guided mode resonances (GMRs) at normal incidence. This coupling confines the electric field within the thin film, significantly boosting the nonlinear interaction. GMR excitation has been investigated in dielectric and plasmonic gratings, and Bragg cavities [17–20]. While these structures offer higher conversion efficiencies and compatibility with free-space collection, they provide limited spatial control over the emitted SH.

A promising direction to combine field confinement with additional degrees of freedom for polarization and spatial control over the nonlinear interaction involves exciting GMRs with metasurfaces. Recently, dielectric metasurface-coupled GMRs in $LiNbO_3$ structures were studied, demonstrating among the best conversion efficiencies for such free space devices [21,22].

In this work, we investigate the use of plasmonic metasurfaces consisting of a collection of nanoantennas to enable efficient coupling into GMRs and enhance the nonlinear interaction. Plasmonic nanoantennas provide strong spectral and polarization tunable scattering, as well as near-field hot spots, however, at the cost of increased absorption. By spectrally detuning the localized surface plasmon resonance from the GMR, we mitigate the plasmonic absorption and obtain tunable control over the resonance quality factor. This results in strong and angularly tunable enhancement of the SHG.

2. Results

The proposed metasurface–waveguide hybrid system is schematically illustrated in Fig. 1(a). It consists of a 900 nm thick X-cut $LiNbO_3$ film on a fused silica substrate. A gold metasurface composed of nanorod antennas is fabricated on top of the film. The system is excited by a plane wave incident from the metasurface side. Due to the design of the metasurface, the incident light couples into guided mode resonances in the thin film. The antennas are oriented along the Z-axis of the crystal, enabling diffraction only in the Y-direction and coupling to the fundamental TE_0 mode. This configuration effectively confines the electric field and aligns it with the d_{33} component of the $\chi^{(2)}$ tensor, thereby maximizing second-harmonic generation (SHG) efficiency. The generated SHG signal is collected from the substrate side.

The gold nanoantennas are arranged in a rectangular lattice with periodicities of a_y = 730 nm and a_z = 220 nm, engineered to support a dominant guided mode resonance at a wavelength of about 1500 nm. To verify that this geometric configuration indeed supports the desired modal structure, we employ analytical estimates based on a slab waveguide model. Since for these parameters diffraction occurs only along the y-direction, we focus only on TE modes, and solve

Optical Materials EXPRESS

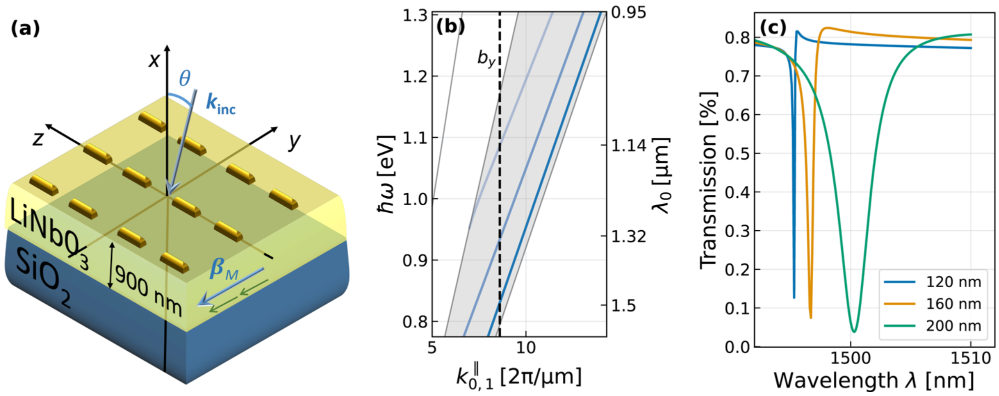

Fig. 1. (a) General layout of the structure. Light at free space wavelengths around 1500 nm is coupled to the GMR through the metasurface, the transmitted SH is collected from the substrate side. (b) Waveguide dispersion from the analytical solution in Eq. (1), showing the dispersion of the TE_0, TE_1 and TE_2 guided modes. The dashed line represent dispersion solution for the light at the fundamental frequency, normal incidence and first order diffraction ($k^{\parallel}_{\text{inc}} = 0; \beta_M = b_y$).(c) Simulated spectral transmission at normal incidence showing the dependence of the TE_0 resonance position on antenna length for the $a_y = 730$ nm and $a_z = 220$ nm lattice. The Q-factor decreases from ~ 14,000 for 120 nm long antennas to ~ 2800 for 160 nm and ~ 470 for 200 nm antennas.

the respective standard transcendental equation:

$$\text{TE} : \tan(\kappa_M h) = \frac{\kappa_M(\gamma_M + \delta_M)}{\kappa_M^2 - \delta_M \gamma_M} \tag{1}$$

where $\kappa_M = \sqrt{\varepsilon_{\text{core}} k_0^2 - \beta_M^2}$, $\delta_M = \sqrt{\beta_M^2 - \varepsilon_{\text{sub}} k_0^2}$ and $\gamma_M = \sqrt{\beta_M^2 - \varepsilon_{\text{sup}} k_0^2}$. Here, h is the slab's thickness, k_0 is the wavenumber in vacuum, and $\varepsilon_{\text{core}}$, ε_{sub}, and ε_{sup} denote the dielectric permittivities of the core, substrate, and superstrate, respectively. The propagation constant β_M is derived from in-plane diffraction as:

$$\beta_M = k^{\parallel}_{m_x,m_y} = k^{\parallel}_{\text{inc}} + m_x b_x + m_y b_y \tag{2}$$

where $b_{x,y}$ are the primitive reciprocal lattice vectors, $m_{x,y}$ are integers denoting the diffraction order, k_{inc} and k_{m_x,m_y} are the incident and the diffracted wave vectors, respectively, and the superscript $\parallel$ indicates the vector's projection on the metasurface plane. At normal incidence ($k^{\parallel}_{\text{inc}} = 0$) and for first-order diffraction along the y direction ($m_{x,y} = \pm 1$), this model predicts resonance wavelengths of approximately 1500 nm (TE_0), 1320 nm (TE_1), and 1150 nm (TE_2). These predictions are shown in Fig. 1(b), and provide a theoretical basis for the design and mode identification discussed later in the experimental results.

To avoid destructive interference of the GMRs with the localized surface plasmon resonance (LSPR) of the antennas, the system is operated in an off-plasmon-resonance regime [23], where the LSPR is spectrally detuned from the guided mode resonance. Spectral detuning is controlled by varying the antenna dimensions: shortening the antennas blue-shifts the LSPR and increases its separation from the guided mode resonance, whereas elongating them brings the two resonances closer. This detuning serves as an effective means of controlling and improving the quality factor (Q-factor) of the guided mode. When the LSPR and GMR are spectrally close, the coupling is enhanced, resulting in a broadened resonance and a reduced Q-factor. Conversely, increased spectral separation suppresses the coupling, yielding a narrower resonance with a higher Q-factor.

Optical Materials EXPRESS

These trends are validated by linear numerical simulations performed in COMSOL (see Methods), as shown in Fig. 1(c).

While a higher Q-factor is beneficial for enhancing the light–matter interaction and second-harmonic generation efficiency, it also increases the system's sensitivity to fabrication imperfections, inhomogeneity and optical losses, particularly in the case of smaller antennas. Therefore, to satisfy fabrication constraints while maintaining good optical performances, we chose antenna dimensions of 160 length and 60 nm width and height. This configuration positions the LSPR at approximately 1100 nm, sufficiently detuned from the 1500 nm GMR to avoid resonance overlap. According to numerical simulations (detailed information can be found in the Methods section) of the optimized system, this design can potentially yield a SHG conversion efficiency $\eta = 2.6 \times 10^{-2}$ for incident fundamental intensity of $1.25\,\mathrm{GW\,cm^{-2}}$.

For the experimental characterizations, we fabricated the sample using a standard electron-beam lithography process. Detailed information about the fabrication process and the experimental setup is described in the Methods section. Figure 2(a) presents the measured linear transmittance spectrum, which shows close agreement with numerical simulations. We observe a significant broadening of the experimentally assessed TE_0 guided mode, featuring a Q factor of approximately 76 (compared to a simulated value of ~ 2800), along with a reduction in coupling efficiency. These effects are attributed primarily to fabrication-induced deviations in the shape and orientation of the antennas, as evident in the scanning electron microscope (SEM) image shown in Fig. 2, as well as to possible differences in the imaginary part of the dielectric function of gold in the nanostructures [24]. Additional broadening arises from finite-beam excitation using a weakly focused Gaussian beam with a diameter comparable to the metasurface dimensions. The LSPR induced broadening of the GMR and their interference can be also seen for the TE_1 and TE_2 GMRs.

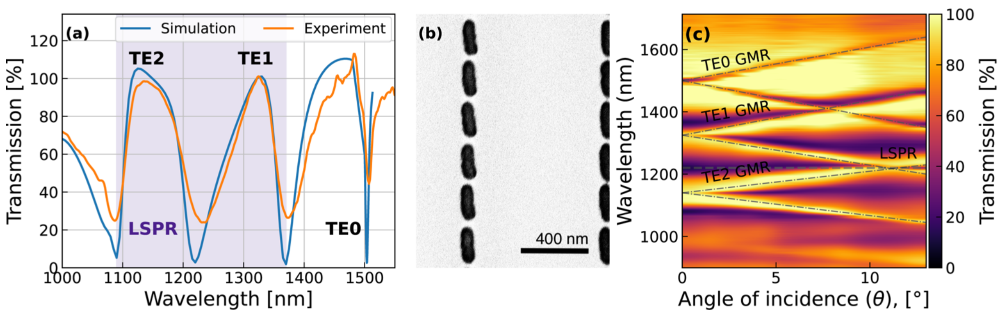

Fig. 2. (a) Simulated and measured spectrum of the sample normalized to the plane film transmission at the normal incidence. The shaded region indicates the localized surface plasmon resonance (LSPR) of the antennas. (b) SEM imaging of the fabricated sample. (c) Angle-dependent transmission measurements.

To further investigate the GMRs, angle-resolved transmittance measurements were conducted, as shown in Fig. 2(c). A broad absorption band can be seen from 1100 nm to 1350 nm corresponding to the localized surface plasmon resonance, which remains independent of the incidence angle, but shows interference with the dispersive GMRs. This is expected, as the LSPR is determined by the geometric dimensions of the nanoantennas and is not affected by angular tuning. Three distinct guided mode resonances are observed to split and shift spectrally with increasing angle. These are identified as the TE_0, TE_1, and TE_2 modes, appearing at wavelengths consistent with the analytically predicted positions shown in Fig. 1(b).

At normal incidence, the TE_1 and TE_2 resonance spectrally interfere with the LSPR, resulting in antireflection effect and transmittance values exceeding 100%, when normalized to the transmittance of the bare $LiNbO_3$ film. By increasing the incidence angle, the GMRs can be

Optical Materials EXPRESS

tuned away from the LSPR. For instance, at 8° incidence, the TE_1 resonance shifts to 1420 nm, moving out of the spectral range of the LSPR and exhibiting a conventional coupling.

These experimental results confirm the tunable nature of the proposed system, both in the design stage and in practical implementation, and demonstrate good agreement with the simulated behavior.

As the next step, nonlinear measurements were conducted to evaluate the second-harmonic generation response of the system (see Methods). As shown in Fig. 3(a), the SH signal from the metasurface exhibits a thirteen-fold enhancement compared to the bare thin film. Figure 3(b) shows the SH spectrum for increasing pump power and Fig. 3(c) represent peak SH counts vs. FH power in logarithmic scale, showing the quadratic dependence of the SH signal on input power, as expected for second-order order nonlinear process.

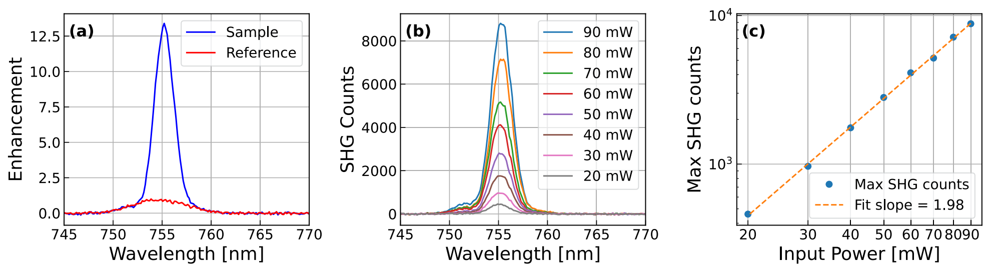

Fig. 3. (a) Second-harmonic spectra from the metasurface sample compared with the bare lithium niobate thin film. (b) Evolution of the SH spectrum with increasing fundamental-harmonic input power, demonstrating consistent spectral shape and power-dependent scaling. (c) Power dependence of the peak SH counts, plotted on a log–log scale with a linear fit slope of ~2.

To demonstrate the spectral tuning of the SH enhancement, we performed angle-dependent measurements. Figure 4(a) shows the SH enhancement obtained by tilting the incidence angle up to 3°, demonstrating a wavelength dependence consistent with the angular dispersion arising from the change in the in-plane propagation constant. In this manner, the guided mode resonance was tuned by approximately 100 nm at the fundamental wavelength, corresponding to a ~ 50 nm shift in the second-harmonic signal, while preserving a comparable enhancement level. Minor variations in SHG efficiency are attributed to factors such as fluctuations in the input beam during OPO tuning and beam path deviations due to angular adjustments. Further red-shifted tuning is not shown experimentally due to the limited tuning spectral range of the fs laser, although in principle it can be extended further into infrared.

Figure 4(b) shows that the bandwidth of the fs laser (see the Method section) has a limited spectral overlap with the guided mode resonance. The FWHM of the SH due to the guided mode resonance is 2.24 nm, whereas that measured from the bare film is 6.26 nm. This suggests that approximately 36% of the input power is spectrally coupled into the resonance, leading to reduced SHG conversion efficiency.

To improve the spectral overlap between the excitation pulse and the guided mode resonance, we conducted additional measurements using a picosecond optical paremateric amplifier (OPA) source with a spectral bandwidth of 1.3 nm (see Methods). As demonstrated in Fig. 4(c), this leads to uniform enhancement across all spectral components of the excitation pulse, yielding a 22-fold enhancement of the SH. Measurements of conversion efficiency with this system yield absolute conversion efficiencies of $\eta_{abs} = 1.35 \times 10^{-5}$ at a fundamental peak intensity of $1.2\,GW\,cm^{-2}$. Importantly, if we compare the enhancement over the full bandwidth of the pulses, for the femtosecond case we get an average enhancement of 5.8, whereas for the picosecond we observe a 22-fold enhancement, further emphasizing the importance of mode matching.

Optical Materials EXPRESS

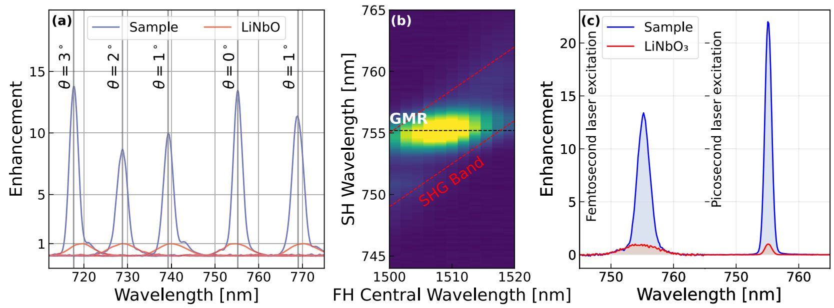

Fig. 4. (a) GMR tunning and corresponding SH enhancement by changing the incident angle. (b) Second-harmonic spectrum as a function of the FH central wavelength. The red lines delimit the FWHM bandwith of the SH signal from the unpatterned film. (c) Comparison of the SH spectrum under 1508 nm FH excitation using a femtosecond OPO (left) and a picosecond OPA (right).

3. Conclusions

We have demonstrated a metasurface–waveguide hybrid platform based on lithium niobate on insulator (LNOI) for enhanced second-harmonic generation (SHG) via excitation of the guided mode resonances (GMRs). Importantly, we design the system to work in the off-plasmonic-resonant regime, enabling spectral control of the resonance quality factor. Experimental measurements revealed a 22-fold nonlinear enhancement and ∼ 100 nm angular tunability of the guided mode resonance. The experimental spectral results are in good agreement with both the simulations and the analytical predictions. However, the measured conversion efficiency of 1.35×10^{-5} is around three orders of magnitude lower than predicted by simulations. This deviation arises from differences in the experimental and simulated quality factors of the GMR at the fundamental frequency, given that SHG efficiency scales quadratically with the Q factor. Comparing the differences in quality factors we get $(Q_{\text{sim}}/Q_{\text{exp}})^2 \approx 1350$ which explains the observed three-order-of-magnitude reduction in conversion efficiency. This indicates that the experimental conversion efficiency can be considerably improved by improving antenna fabrication and bringing the experiential quality factor closer to the theoretical predictions. Moreover, the quality factors can be further improved by design [23] to aim towards more efficient SHG from the system. In this work, a 900 nm thick TFLN film was used, however, the results are applicable to other TFLN thicknesses, and the conversion efficiency may be further optimized by studying the effect of film thickness. As a possible future direction, similar design concepts could be applied to quasi-BIC and quasi-guided mode resonances, where the resonance quality factor is determined by symmetry breaking or subwavelength perturbations rather than by the spectral position of the LSPR. Such strategies would allow independent control over the Q-factor and spectral tuning, enabling further enhancement of nonlinear performance while maintaining compatibility with plasmonic fabrication accuracy. Altogether, this work demonstrates the potential of plasmonic metasurfaces in this configuration, and can be further enhanced to combine concepts of non-local spatial and spectral control for SHG [25].

4. Methods

4.1. Simulations

Numerical simulations were performed using COMSOL Multiphysics by modeling a single unit cell with Floquet periodic boundary conditions. The structure was excited with an ideal plane wave at a power of 2 W per lattice period, launched through a port located on the substrate side. Transmitted and second-harmonic (SH) powers were calculated by integrating the corresponding

Optical Materials EXPRESS

fields over a second port located 900 nm above the metasurface in the air. Nonlinear simulations were carried out by implementing the second-order nonlinear susceptibility tensor in the $LiNbO_3$ domain. The undepleted pump approximation was employed.

4.2. Fabrication and measurements

The LNOI wafer was purchased from NANOLN. A 100 µm × 100 µm square metasurface pattern was defined by electron-beam lithography (RAITH 150 II) using A4 PMMA as the resist. After the development, a 5 nm titanium adhesion layer and a 55 nm gold layer were successively deposited by electron beam evaporation. Lift-off was performed in acetone to remove the residual PMMA.

Both linear and nonlinear measurements were performed on the same optical setup. For linear characterization, a SuperK COMPACT white laser source by NKT and an NIRQuest infrared spectrometer by Ocean Optics were used. For nonlinear measurements, a Chameleon OPO-Vis by Coherent (140 fs pulse duration, 80 MHz repetition rate) served as the excitation source, and SHG was detected using an Avantes high resolution fiber-coupled spectrometer. A 200 mm focal length lens was used to weakly focus the fundamental beam onto the sample. To examine the effect of mode matching, measurements in a similar setup with the same focusing lens and spectrometer were performed using ORPHEUS picosecond OPA (1800 fs pulse duration, 33 kHz repetition rate).

For efficiency calculations, the input power was measured directly before the sample using a thermopile sensor, and the SH power was recorded with a silicon photodiode sensor placed after the collection lenses and before the spectrometer. A consistency check was carried out to verify that both sensors reported the same power under identical excitation conditions. The reported conversion efficiency accounts for reflection losses from the optical elements in the detection path.

Funding. European Research Council (ERC 3D NOAM 101044797); Italian Ministry of University and Research (MUR) (PRIN 2022 "No LIMITHz", 2022BC5BW5; CUP D53D23001130006).

Disclosures. The authors declare no conflict of interest.

Data availability. Data underlying the results presented in this paper are not publicly available at this time but may be obtained from the authors upon reasonable request.

References

1. L. Qu, W. Wu, W. Cai, *et al.*, "Second Harmonic Generation in Lithium Niobate on Insulator," Laser Photonics Rev. **19**(11), 2401928 (2025).
2. D. Zhu, L. Shao, M. Yu, *et al.*, "Integrated photonics on thin-film lithium niobate," Adv. Opt. Photonics **13**(2), 242 (2021).
3. S. Saravi, T. Pertsch, and F. Setzpfandt, "Lithium Niobate on Insulator: An Emerging Platform for Integrated Quantum Photonics," Adv. Opt. Mater. **9**(22), 2100789 (2021).
4. A. Honardoost, K. Abdelsalam, and S. Fathpour, "Rejuvenating a Versatile Photonic Material: Thin-Film Lithium Niobate," Laser Photonics Rev. **14**(9), 2000088 (2020).
5. H. Li, W. Liu, Z. Wu, *et al.*, "Nonlinearity manipulation for highly efficient modal phase-matched second harmonic generation on thin-film lithium niobate," Laser Photonics Rev. **19**(8), 2401858 (2025).
6. C. Wang, C. Langrock, A. Marandi, *et al.*, "Ultrahigh-efficiency wavelength conversion in nanophotonic periodically poled lithium niobate waveguides," Optica **5**(11), 1438 (2018).
7. C. Lu, Y. Zhang, J. Qiu, *et al.*, "Highly tunable birefringent phase-matched second-harmonic generation in an angle-cut lithium niobate-on-insulator ridge waveguide," Opt. Lett. **47**(5), 1081 (2022).
8. M. Li, H. Liang, R. Luo, *et al.*, "High-Q 2D lithium niobate photonic crystal slab nanoresonators," Laser Photonics Rev. **13**(5), 1800228 (2019).
9. J. Wang, B. Wang, J. Qu, *et al.*, "Second harmonic and sum frequency generation in silicon nitride microring on thin-film lithium niobate," Opt. Lett. **50**(6), 2057 (2025).
10. L. Carletti, A. Zilli, F. Moia, *et al.*, "Steering and Encoding the Polarization of the Second Harmonic in the Visible with a Monolithic $LiNbO_3$ Metasurface," ACS Photonics **8**(3), 731–737 (2021).
11. Y. Liu, B. Wang, L. Hu, *et al.*, "Observation of Anapole Resonances in Lithium Niobate Metasurfaces with Significantly Enhanced Second Harmonic Generation," Adv. Mater. Technol. **9**(22), 2400318 (2024).

Optical Materials EXPRESS

12. A. Di Francescantonio, A. Sabatti, H. Weigand, *et al.*, "Efficient GHz electro-optical modulation with a nonlocal lithium niobate metasurface in the linear and nonlinear regime," Nat. Commun. **16**(1), 7000 (2025).
13. J. Zhang, J. Ma, M. Parry, *et al.*, "Spatially entangled photon pairs from lithium niobate nonlocal metasurfaces," Sci. Adv. **8**, abq4240 (2022).
14. M. A. Weissflog, J. Ma, J. Zhang, *et al.*, "Directionally tunable co- and counterpropagating photon pairs from a nonlinear metasurface," Nanophotonics **13**(18), 3563–3573 (2024).
15. L. Qu, L. Bai, C. Jin, *et al.*, "Giant Second Harmonic Generation from Membrane Metasurfaces," Nano Lett. **22**(23), 9652–9657 (2022).
16. Z. Li, X. Ye, Z. Hu, *et al.*, "Plasmonic hotspot arrays boost second harmonic generation in thin-film lithium niobate," Opt. Express **32**(8), 13140 (2024).
17. Y. Hu, Z. Huang, X. Zeng, *et al.*, "Resonant nonlinear nanostructured grating in an unstructured lithium niobate on insulator platform," Opt. Mater. Express **13**(10), 2904 (2023).
18. Y. Ju, W. Zhang, and H. Zuo, "Promoting second-harmonic generation in the LiNbO3 film combined with metasurface using plasmonic quasi bound states in the continuum," Photonics and Nanostructures - Fundamentals and Applications **57**, 101194 (2023).
19. Y. Zhao, Z. Chen, C. Wang, *et al.*, "Efficient second- and higher-order harmonic generation from $LiNbO_3$ metasurfaces," Nanoscale **15**(31), 12926–12932 (2023).
20. Z. Li, Z. Hu, X. Ye, *et al.*, "Enhanced Second-Harmonic Generation in Thin-Film Lithium Niobate Circular Bragg Nanocavity," Nano Lett. **24**(37), 11676–11682 (2024).
21. H. Jiang, K. Sun, Y. Jia, *et al.*, "Tunable Second Harmonic Generation with Large Enhancement in A Nonlocal All-Dielectric Metasurface Over A Broad Spectral Range," Adv. Opt. Mater. **12**(17), 2303229 (2024).
22. Z. Wang, B. Li, N. Lu, *et al.*, "Highly Efficient Ultraviolet Harmonic Generation Based on Coupled Guided Mode Resonances in Lithium Niobate Metasurfaces," Laser Photonics Rev. **19**(22), e01010 (2025).
23. M. S. Bin-Alam, O. Reshef, Y. Mamchur, *et al.*, "Ultra-high-Q resonances in plasmonic metasurfaces," Nat. Commun. **12**(1), 974 (2021).
24. M. Celebrano, M. Savoini, P. Biagioni, *et al.*, "Towards the epitaxial growth of Au thin films on MgO substrates for plasmonic applications," J. Eur. Opt. Society-Rapid Publ. **20**(1), 12 (2024).
25. A. Overvig and A. Alú, "Diffractive Nonlocal Metasurfaces," Laser Photonics Rev. **16**(8), 2100633 (2022).